NANO LETTERS

Letter

pubs.acs.org/NanoLett

Indication of Complete Spin Filtering in Atomic-Scale Nickel Oxide

Ran Vardimon,* Marina Klionsky,* and Oren Tal*

Department of Chemical Physics, Weizmann Institute of Science, Rehovot 76100 Israel

Supporting Information

ABSTRACT: Generating highly spin-polarized currents at the nanoscale is essential for spin current manipulations and spintronic applications. We find indications for up to 100% spin-polarized currents across nickel oxide atomic junctions formed between two nickel electrodes. The degree of spin polarization is probed by analyzing the shot noise resulting from the discrete statistics of spin-polarized electron transport. We show that spin filtering can be significantly enhanced by local chemical modifications at the single-atom level. This approach paves the way for effective manipulations of spin transport at the fundamental limit of miniaturization.

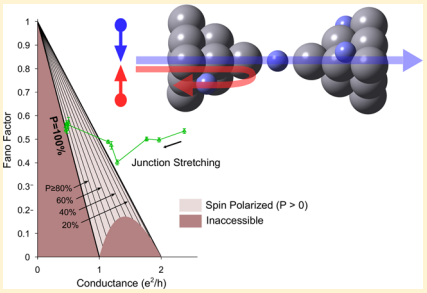

KEYWORDS: *Spintronics, molecular electronics, spin filtering, magnetoresistance, atomic contact, spin-polarized transport*

While conventional electronics is based on the charge of electrons, exploiting the additional spin degree of freedom offers advantages for electronics and computing applications.[1] Perhaps the most central requirement for the efficient operation of spin-based devices is the ability to generate a highly spin-polarized current governed by electrons of a single spin type. The design of materials that promote spin filtering is a promising approach as demonstrated by the highly spin-polarized currents measured in structures based on several half-metallic compounds.[2,3] However, when the system size is decreased toward the nanoscale, achieving high spin polarization becomes increasingly challenging. At very small length scales, structural modifications as well as mixing between bulk and surface properties can substantially deteriorate spin selectivity. Alternative schemes explored at the nanoscale include atomic and molecular junctions based on ferromagnetic metals.[4−11] Nickel, iron, and cobalt are easily shaped even at the nanoscale while preserving useful magnetic properties and a well-defined chemical composition. Unfortunately, electronic transport in these ferromagnets is dominated by weakly spin-polarized s bands, leading to limited spin-polarized conduction in related nanoscale devices.[12,13] A number of experiments applying scanning tunneling microscopy were able to locally probe the magnetoresistance effect in ferromagnetic substrates involving adsorbed atoms[10] or molecules.[7,9,14−16] The magnetoresistance values reported have ranged around several tens of percent, suggesting partially spin-polarized transport. In a recent work,[17] the degree of spin polarization was probed directly using the Meservey−Tedrow−Fulde effect.[18] For example, the polarization for bilayer Co islands showed an enhancement to 65% compared to previous measured values of 35% for bulk Co.[18] Nevertheless, obtaining complete spin filtering in ferromagnetic based nanoscale devices has been so far elusive.

Here, we present experimental results indicating that up to 100% spin-polarized currents can be realized at the ultimate size limit of an atomic conductor formed between two ferromagnetic electrodes. When current passes through an atomic-sized constriction, quantum confinement dictates that electronic transport is governed by the fine details of the local electronic structure. Suitable atomistic conditions can also affect the balance between spin-up and spin-down currents, as recent theoretical[19] and experimental[20−22] works have suggested. We take advantage of this sensitivity to efficiently manipulate spin-dependent transport by modifying the structure and composition of an atomic-scale conductor. We find that the formation of a nickel oxide (NiO) atomic junction between two nickel electrodes leads to highly efficient spin filtering that allows only one spin-type to flow through the constriction (Figure 1a). In accordance with recent *ab initio* calculations,[23,24] our findings are explained in view of the orbital hybridization between low-coordinated Ni and O atoms, resulting in the emergence of local half-metallicity.

We investigated electronic spin transport in NiO junctions, formed in cryogenic conditions (4.2 K) using a break-junction setup. As a first step, Ni atomic junctions were created by breaking a Ni wire using a 3-point bending mechanism driven by a piezoelectric element (Figure 1b). During the breaking process the conductance drops in sudden steps as the number of atoms in the narrowest cross-section of the contact is reduced.[25,26] The evolution of the Ni atomic junction is characterized by recording the conductance vs interelectrode displacement during thousands of repeated breaking cycles. Before the wire fully breaks, a single atom junction is formed, resulting in a short conductance plateau (Figure 1c). As indicated by the conductance histogram (Figure 1d, inset) and the 2D density plot (Figure 1d) that are constructed from an ensemble of conductance traces, the typical conductance for the

Received: February 23, 2015
Revised: April 22, 2015

DOI: 10.1021/acs.nanolett.5b00729
Nano Lett. XXXX, XXX, XXX−XXX

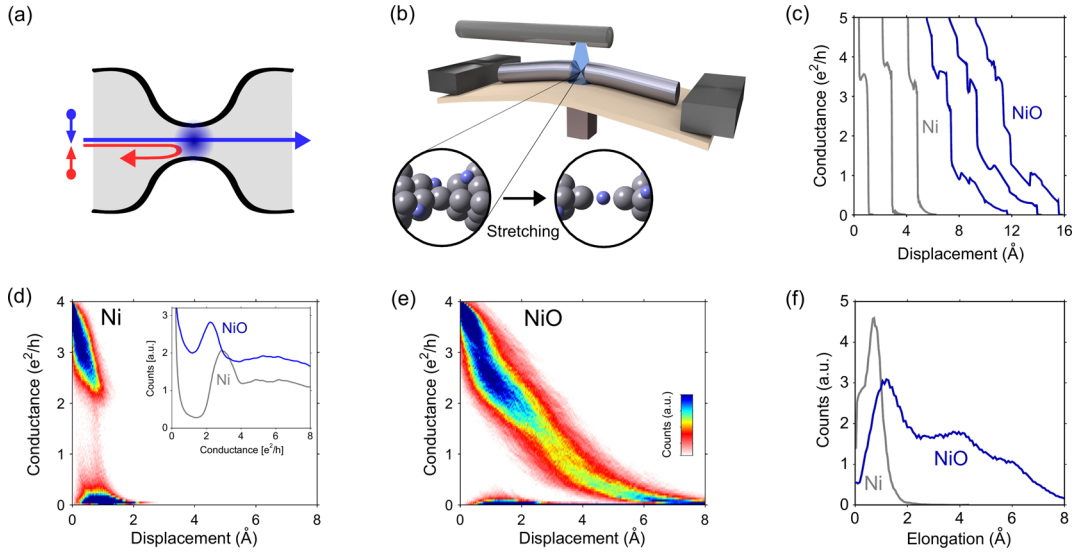

Figure 1. (a) Schematic illustration of spin-filtering by a NiO atomic constriction between two Ni electrodes. (b) Schematic illustration of *in situ* formation of a NiO atomic junction within the mechanical break junction setup. (c) Example conductance traces recorded for a bare Ni contact (gray) and after the insertion of oxygen (blue). Traces are shifted in the displacement axis for clarity. (d,e) Density plots of conductance vs interelectrode displacement for Ni atomic junctions, before (d) and after the introduction of oxygen (e). Inset of (d) shows the corresponding conductance histograms for Ni (gray) and NiO (blue). The density plots are constructed from 10,000 Ni and 10,000 NiO traces that were aligned from the first value below $4e^2/h$. (f) Length histograms for Ni (gray) and NiO (blue) atomic-scale junctions (see text).

single-atom junction is $2 - 4e^2/h$ (e^2/h is the spin-resolved conductance quantum denoted below as G_q) in accordance with previous studies.[13,27,28]

Following the formation of atomic-scale Ni junctions, oxygen was introduced to the junction via a heated capillary (Figure 1b). Conductance traces recorded subsequently show a distinct behavior (Figure 1c). While the exact atomic geometry of the junction can vary at each breaking cycle, several repeating key features are revealed by statistical analysis of the data (Figure 1d–f), allowing us to determine the main characteristics of the atomic structure: (i) In contrast to the case of bare Ni junctions, conductance lower than $2e^2/h$ is frequently observed. The appearance of new conductance values before rupture indicates that oxygen is incorporated into the narrowest cross-section of the junction, which comprises the resistive bottleneck for electronic transport.[25,29,30] (ii) The frequent appearance of conductance values associated with a single Ni atomic junction is maintained despite the appearance of new features at lower conductance (Figure 1e). This indicates that oxygen is drawn to form an atomic junction only after the Ni atomic junction is formed. (iii) Molecular oxygen is known to dissociate and chemisorb on Ni surfaces, even at cryogenic temperatures.[31,32] We find evidence for oxygen dissociation in the dramatic increase of the junction elongation. While Ni junctions sustain an elongation of ~1 Å at the most, the oxidized junction can be pulled apart by up to 8 Å, equivalent to several times the interatomic distance of bulk Ni (2.49 Å).[33] The length histogram presented in Figure 1f describes the distribution of junction elongations from $4e^2/h$ until rupture. The histogram shows a series of peaks with interpeak displacement of ~2.4 Å, indicating elongation by a repeated atomic unit. The increased elongation and appearance of the peak structure indicate the formation of NiO atomic chains, as reported for different metal oxides.[26,30] Altogether, these observations point out to the insertion of atomic oxygen into the Ni junction (i.e., Figure 1b), which can be followed by the formation of oxygen incorporated atomic chains. As will be shown, this conclusion is further supported by the good agreement of our electronic transport measurements with first-principles and transport calculations on similar modeled structures.

In order to detect spin-dependent transport, we turn to investigate the electronic shot noise generated by our junctions. The study of shot noise has shown to be useful for revealing underlying spin transport mechanisms for various systems.[22,34−36] As will be shown in the following, conductance and shot noise data can be used to obtain a quantitative estimation of the current spin polarization. We note that the significant advantage of this measurement is the local probing of the spin-polarization at the resistive atomic constriction, which dominates the noise signal. The quantum nature of transport through atomic-scale constrictions is reflected in the conductance $G = G_q \Sigma\tau_{n,\sigma}$, which takes place through N discrete conduction channels of each spin type $\sigma = \uparrow$ *or* $\downarrow$ with transmission probabilities $\tau_{n,\sigma}$ $(1 \le n \le N)$.[37] We define the absolute spin polarization as $P = |G_\uparrow - G_\downarrow|/G$, where $G_\sigma = G_q \Sigma_n \tau_{n,\sigma}$. From shot noise measurements one can gain additional information regarding the distribution of $\tau_{n,\sigma}$, which in turn can be used to evaluate P. For the case of two channels with opposite spins, one obtains

$$F = 1 - \frac{1 + P^2}{2}\frac{G}{G_q} \tag{1}$$

Here $F = \Sigma\tau_{n,\sigma}(1 - \tau_{n,\sigma})/\Sigma\tau_{n,\sigma}$ is the Fano factor, which is equal to the shot noise in units of $2eI$ (I is the current). P can be uniquely determined from the measured values of F and G. For the general case of a variable number of spin channels, it can be shown that the spin polarization is necessarily equal or higher than the P obtained using eq 1 (Supplementary Section S5). We take advantage of this behavior to draw a lower bound for the spin polarization of the current across NiO junctions. This approach can be visualized in the (F,G) space (Figure 2a) as following. Two important regions can be identified: (i) the inaccessible region (dark shaded area) in which no solutions for

DOI: 10.1021/acs.nanolett.5b00729
Nano Lett. XXXX, XXX, XXX−XXX

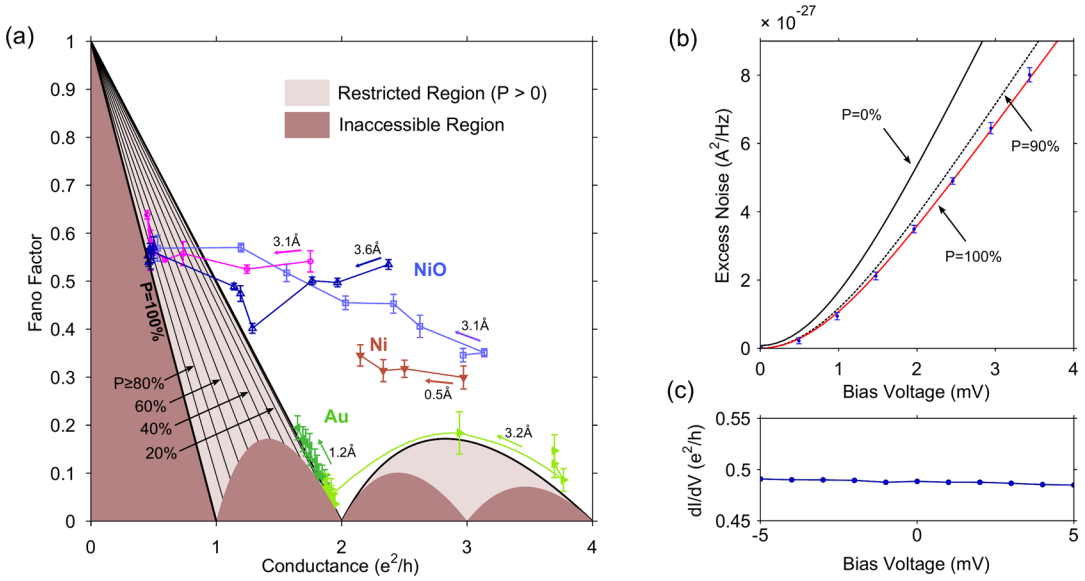

Figure 2. (a) Evolution of Fano factor (F) and conductance (G) recorded during elongation of NiO junctions (empty circles, squares, and triangles, colored in blue, purple and pink), bare Ni (face down filled triangles, red), and Au (side-facing filled triangles, green). The total elongation is indicated for each sequence. Upon junction stretching, the measured values for NiO gradually penetrate the region that indicates spin-polarized transport (light shaded area), showing an increasing degree of spin polarization (indicated by black lines) up to 100% spin polarization for measured (F,G) on the boundary of the region that is inaccessible for all measurements (dark shaded area). (b) Bias dependence of the excess noise $S(V) - S(V = 0)$ for an elongated NiO junction ($G = 0.49 \pm 0.01e^2/h$, $F = 0.53 \pm 0.02$). Red line shows the calculated noise for a single spin channel ($\tau = 0.49$; $P = 100\%$). Black lines show the calculated noise for two channels with $\tau_1 + \tau_2 = 0.49$ and $P = 0\%$ (solid) or $P = 90\%$ (dashed). (c) dI/dV curve measured for the same junction that is analyzed in (b).

(F,G) exist; and (ii) the restricted region (light shaded), where necessarily $P > 0$. Following eq 1, measured values located below one of the solid lines in the restricted region indicate that P is greater than the value indicated on the line.

Figure 2a shows the evolution of F and G throughout the elongation of atomic junctions with different atomic composition. Following each elongation step, the electrode separation was kept constant, and a series of noise measurements as a function of bias was performed. The value of F was determined from the noise dependence on bias voltage (Supplementary Section S3). For nonmagnetic atomic junctions of Au the data points follow the outer boundary of the restricted region. The suppression of shot noise to the minimal value allowed for a spin-degenerate system reflects the monovalent s character of Au.[38] For Ni junctions, although transport is expected to be moderately spin-polarized, the data points are found higher away from the restricted region. This is indeed likely when the conductance is carried by several partly transmitting channels,[13,36] as was also found for other transition d metals.[29,39] Three different elongation sequences are presented for oxidized Ni junctions, starting from conductance values associated with a single-atom Ni junction ($\sim 2 - 4e^2/h$). As the contact is pulled apart and an NiO junction is formed, the data points penetrate the restricted region. Remarkably, after elongation of about 1−2 Å, the conductance is found to be highly spin-polarized, with P values reaching 95−100%. The values of F and G are rather insensitive to further elongation, indicating that the high spin polarization is preserved by the formation of a stable atomic structure. From analysis of 212 shot noise measurements on junctions with $G < 1e^2/h$, we find that 9% of the junctions exhibit a spin polarization larger than 90%. For nearly half of the measurements (46%), the spin polarization is found to be at least 50% (see Supplementary Section S4). As different atomic configurations are probed throughout our measurements, these results indicate that the appearance of a certain degree of spin-filtering effect is fairly robust to junction geometry.

Figure 2b shows an example for the bias voltage dependence of the noise measured for an elongated junction. The data agrees very well with the expected shot noise for a single spin channel (P = 100%; red line) using no fitting parameters. Lower values of P would necessarily result in a higher Fano factor, leading to distinguishable noise dependence on bias. This is exemplified for a hypothetic case of two channels assuming either P = 90% (dashed black line) or P = 0% (solid black line). The zero-bias conductance used here is obtained from the dI/dV spectrum in the bias window of 4 mV (Figure 2c).

The origin of the unique spin-transport properties of the studied NiO junctions can be understood in view of selective orbital hybridization between low-coordinated Ni and O atoms. Figure 3a schematically illustrates the main characteristics of the local density of states for Ni and NiO systems, based on former calculations for infinite 1D atomic chains and atomic junction geometries.[13,23,24,28] For bare Ni, the 3d and 4s atomic orbitals have states near the Fermi energy that can contribute several channels to the conductance. The conductance is governed by the virtually unpolarized s bands leading to only moderate spin polarization, consistent with previously reported experimental values that do not exceed ~45%.[2] In contrast, for NiO the hybridization scheme and the associated charge transfer between nickel and oxygen lead to a distinct energetic picture. As a result of the oxidation, the Ni atoms are positively charged, shifting the s states to higher energies. In addition, the limited hybridization of the Ni s orbital with the oxygen p orbitals results in a more energetically localized density of states, which lays high above the Fermi energy. Consequently, the contribution of unpolarized s states to transport is suppressed.

DOI: 10.1021/acs.nanolett.5b00729
Nano Lett. XXXX, XXX, XXX−XXX

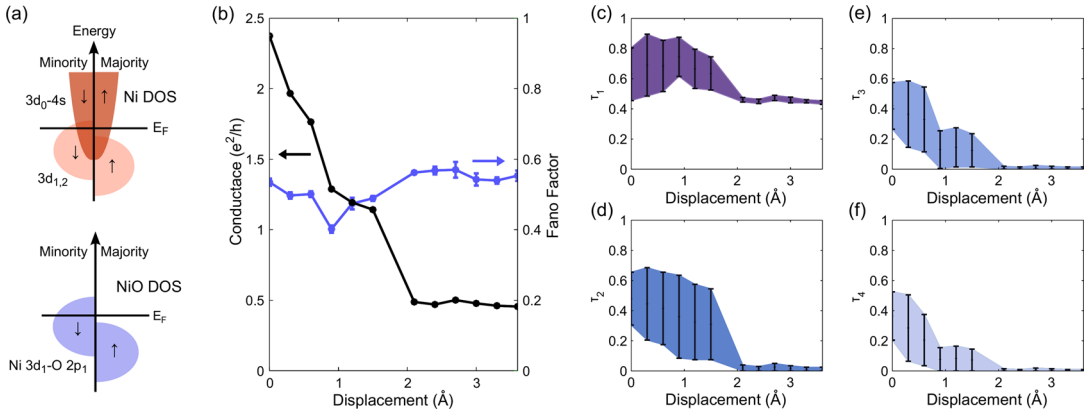

Figure 3. (a) Schematic illustration of the density of states (DOS) for Ni and NiO junctions based on refs 13, 23, 24, and 28. (b) Overall conductance (black) and Fano factor (blue) as a function of interelectrode displacement. (c–f) The individual contributions of spin channels. The four most conducting channels are presented out of six calculated channels. Error bars indicate the numeric uncertainty in determining τ_n.[33]

At the Fermi energy there are contributions from only two minority-spin orbitals, formed by hybridization of two oxygen $2p_1$ orbitals (p_x, p_y, where z is the junction axis) and two nickel $3d_1$ orbitals (d_{xz}, d_{yz}). Furthermore, no majority spin states are available at the Fermi level,[23,24] as the Ni majority-spin d bands are already located at lower energies. Thus, NiO atomic junctions are expected to have a local half-metallic electronic structure, with transport limited to minority spin-channels, leading to an enhanced spin polarization as compared to Ni.

Further insight into the emergence of half-metallicity can be gained by studying the evolution of spin channels during the formation of the NiO junction. To obtain the channel resolution we used a recently introduced numerical analysis of conductance and shot noise data.[38] Figure 3b–f shows the overall conductance, the obtained Fano factor and the contributions from the four most conducting spin channels as a function of interelectrode displacement. At the initial stage of junction elongation, at least four channels are found to significantly contribute to the conductance. Similar channel distributions with $N > 4$–6 channels were also found for bare Ni atomic contacts (Supplementary Section S4), in good agreement with transport calculations.[12,13,28] Thus, at this stage the junction does not show any deviation from the typical characteristics of bare Ni atomic contacts despite the possible presence of adsorbed oxygen.

Following additional elongation of the junction, the number of channels decreases until the conductance is dominated by a single spin channel (Figure 3c). The observed channel-filtering is in good agreement with calculations by Jacob et al. and Rocha et al.[23,24] for a single oxygen atom bridge located between two nickel apexes. The distance in which the channel evolution takes place (~2 Å) is in reasonable agreement with the difference between the calculated Ni atomic separation for Ni–Ni (2.24 Å) and Ni–O–Ni (3.6 Å) configurations. This indicates that efficient spin filtering can be obtained already at a length scale of a single atom. We note that the calculations have found up to two energetically degenerate minority-spin channels for ideal symmetric model structures. However, a removal of degeneracy due to less symmetric junction configurations in experiment is probable, leading to a single spin channel as observed in our measurements.

To conclude, we find that NiO atomic junctions show suppression of shot noise reaching to the minimum value, which is an indication for fully spin-polarized conductance carried by a single spin conduction channel. These findings are consistent with theoretical calculations predicting the emergence of half-metallicity in atomic scale NiO, in contrast to the insulating character of bulk NiO.[23,24] Our results show that a minor change in the local atomic structure, that is, the incorporation of oxygen between the Ni electrodes, can dramatically alter spin-transport properties. Further experimental work on the magnetoresistance effect could serve to expand our understanding regarding the magnetic nature of NiO junctions. Interestingly, theoretical calculations for NiO junctions predict that the resistance change between parallel and antiparallel electrode magnetizations is expected to be several-fold higher compared to bare Ni atomic junctions.[4,5,23,24] The high spin polarization together with the very large current density (~10^{11} A cm^{-2}) make such junctions attractive candidates for realization of atomic-scale spintronic effects, such as significant spin-torque transfer[40] at the ultimate limit for miniaturization.

■ ASSOCIATED CONTENT

Supporting Information

Experimental details on setup and shot noise measurements, further analysis of NiO junctions from conductance vs displacement data, and a mathematical proof for obtaining a lower bound for spin polarization from shot noise data. The Supporting Information is available free of charge on the ACS Publications website at DOI: 10.1021/acs.nanolett.5b00729.

■ AUTHOR INFORMATION

Corresponding Author

*E-mail: oren.tal@weizmann.ac.il.

Notes

The authors declare no competing financial interest.

■ ACKNOWLEDGMENTS

We thank J. M. van Ruitenbeek, S. J. van der Molen, and A. R. Rocha for fruitful discussions. O.T. thanks the Harold Perlman family for their support and acknowledges funding by the Israel Science Foundation and the Minerva Foundation.

■ REFERENCES

(1) Wolf, S. A.; Awschalom, D. D.; Buhrman, R. A.; Daughton, J. M.; Molnár, S.; von Roukes, M. L.; Chtchelkanova, A. Y.; Treger, D. M. *Science* **2001**, *294* (5546), 1488–1495.

DOI: 10.1021/acs.nanolett.5b00729
Nano Lett. XXXX, XXX, XXX–XXX

(2) Soulen, R. J., Jr. *Science* **1998**, *282* (5386), 85−88.
(3) Schmehl, A.; Vaithyanathan, V.; Herrnberger, A.; Thiel, S.; Richter, C.; Liberati, M.; Heeg, T.; Röckerath, M.; Kourkoutis, L. F.; Mühlbauer, S.; Böni, P.; Muller, D. A.; Barash, Y.; Schubert, J.; Idzerda, Y.; Mannhart, J.; Schlom, D. G. *Nat. Mater.* **2007**, *6* (11), 882−887.
(4) Viret, M.; Berger, S.; Gabureac, M.; Ott, F.; Olligs, D.; Petej, I.; Gregg, J. F.; Fermon, C.; Francinet, G.; Goff, G. L. *Phys. Rev. B* **2002**, *66* (22), 220401.
(5) Bolotin, K. I.; Kuemmeth, F.; Pasupathy, A. N.; Ralph, D. C. *Nano Lett.* **2006**, *6* (1), 123−127.
(6) Keane, Z. K.; Yu, L. H.; Natelson, D. *Appl. Phys. Lett.* **2006**, *88* (6), 062514.
(7) Brede, J.; Atodiresei, N.; Kuck, S.; Lazić, P.; Caciuc, V.; Morikawa, Y.; Hoffmann, G.; Blügel, S.; Wiesendanger, R. *Phys. Rev. Lett.* **2010**, *105* (4), 047204.
(8) Egle, S.; Bacca, C.; Pernau, H.-F.; Huefner, M.; Hinzke, D.; Nowak, U.; Scheer, E. *Phys. Rev. B* **2010**, *81* (13), 134402.
(9) Schmaus, S.; Bagrets, A.; Nahas, Y.; Yamada, T. K.; Bork, A.; Bowen, M.; Beaurepaire, E.; Evers, F.; Wulfhekel, W. *Nat. Nanotechnol.* **2011**, *6* (3), 185−189.
(10) Néel, N.; Ferriani, P.; Ziegler, M.; Heinze, S.; Kröger, J.; Berndt, R. *Phys. Rev. B* **2012**, *85* (15), 155406.
(11) Yoshida, K.; Hamada, I.; Sakata, S.; Umeno, A.; Tsukada, M.; Hirakawa, K. *Nano Lett.* **2013**, *13* (2), 481−485.
(12) Jacob, D.; Fernández-Rossier, J.; Palacios, J. *Phys. Rev. B* **2005**, *71* (22), 220403.
(13) Häfner, M.; Viljas, J. K.; Frustaglia, D.; Pauly, F.; Dreher, M.; Nielaba, P.; Cuevas, J. C. *Phys. Rev. B* **2008**, *77* (10), 104409.
(14) Bagrets, A.; Schmaus, S.; Jaafar, A.; Kramczynski, D.; Yamada, T. K.; Alouani, M.; Wulfhekel, W.; Evers, F. *Nano Lett.* **2012**, *12* (10), 5131−5136.
(15) Iacovita, C.; Rastei, M. V.; Heinrich, B. W.; Brumme, T.; Kortus, J.; Limot, L.; Bucher, J. P. *Phys. Rev. Lett.* **2008**, *101* (11), 116602.
(16) Atodiresei, N.; Brede, J.; Lazić, P.; Caciuc, V.; Hoffmann, G.; Wiesendanger, R.; Blügel, S. *Phys. Rev. Lett.* **2010**, *105* (6), 066601.
(17) Eltschka, M.; Jäck, B.; Assig, M.; Kondrashov, O. V.; Skvortsov, M. A.; Etzkorn, M.; Ast, C. R.; Kern, K. *Nano Lett.* **2014**, *14* (12), 7171−7174.
(18) Meservey, R.; Tedrow, P. M. *Phys. Rep.* **1994**, *238* (4), 173−243.
(19) Rocha, A. R.; García-suárez, V. M.; Bailey, S. W.; Lambert, C. J.; Ferrer, J.; Sanvito, S. *Nat. Mater.* **2005**, *4* (4), 335−339.
(20) Smogunov, A.; Dappe, Y. J. Symmetry-Derived Half-Metallicity in Atomic and Molecular Junctions. *Nano Lett.* **2015**, *15* (5), 3552−3556.
(21) Loth, S.; von Bergmann, K.; Ternes, M.; Otte, A. F.; Lutz, C. P.; Heinrich, A. J. *Nat. Phys.* **2010**, *6* (5), 340−344.
(22) Burtzlaff, A.; Weismann, A.; Brandbyge, M.; Berndt, R. *Phys. Rev. Lett.* **2015**, *114* (1), 016602.
(23) Jacob, D.; Fernández-Rossier, J.; Palacios, J. J. *Phys. Rev. B* **2006**, *74* (8), 081402.
(24) Rocha, A.; Archer, T.; Sanvito, S. *Phys. Rev. B* **2007**, *76* (5), 054435.
(25) Agraït, N.; Yeyati, A. L.; van Ruitenbeek, J. M. *Phys. Rep.* **2003**, *377* (2−3), 81−279.
(26) Thijssen, W. H. A.; Marjenburgh, D.; Bremmer, R. H.; van Ruitenbeek, J. M. *Phys. Rev. Lett.* **2006**, *96* (2), 026806.
(27) Untiedt, C.; Dekker, D. M. T.; Djukic, D.; van Ruitenbeek, J. M. *Phys. Rev. B* **2004**, *69* (8), 081401.
(28) Pauly, F.; Dreher, M.; Viljas, J. K.; Häfner, M.; Cuevas, J. C.; Nielaba, P. *Phys. Rev. B* **2006**, *74* (23), 235106.
(29) Scheer, E.; Agrait, N.; Cuevas, J. C.; Yeyati, A. L.; Ludoph, B.; Martin-Rodero, A.; Bollinger, G. R.; van Ruitenbeek, J. M.; Urbina, C. *Nature* **1998**, *394* (6689), 154−157.
(30) Thijssen, W. H. A.; Strange, M.; aan de Brugh, J. M. J.; van Ruitenbeek, J. M. *New J. Phys.* **2008**, *10* (3), 033005.
(31) Hsu, Y.; Jacobi, K.; Rotermund, H. H. *Surf. Sci.* **1982**, *117* (1−3), 581−589.
(32) Beckerle, J. D.; Yang, Q. Y.; Johnson, A. D.; Ceyer, S. T. *Surf. Sci.* **1988**, *195* (1−2), 77−93.
(33) Bowen, H. J. M.; Sutton, L. E. *Tables of Interatomic Distances and Configuration in Molecules and Ions*; Chemical Society: London, U.K., 1958.
(34) Roche, P.; Ségala, J.; Glattli, D. C.; Nicholls, J. T.; Pepper, M.; Graham, A. C.; Thomas, K. J.; Simmons, M. Y.; Ritchie, D. A. *Phys. Rev. Lett.* **2004**, *93* (11), 116602.
(35) DiCarlo, L.; Zhang, Y.; McClure, D. T.; Reilly, D. J.; Marcus, C. M.; Pfeiffer, L. N.; West, K. W. *Phys. Rev. Lett.* **2006**, *97* (3), 036810.
(36) Kumar, M.; Tal, O.; Smit, R. H. M.; Smogunov, A.; Tosatti, E.; van Ruitenbeek, J. M. *Phys. Rev. B* **2013**, *88* (24), 245431.
(37) Blanter, Y. M.; Büttiker, M. *Phys. Rep.* **2000**, *336* (1−2), 1−166.
(38) Vardimon, R.; Klionsky, M.; Tal, O. *Phys. Rev. B* **2013**, *88* (16), 161404.
(39) Makk, P.; Csonka, S.; Halbritter, A. *Phys. Rev. B* **2008**, *78* (4), 045414.
(40) Liu, L.; Pai, C.-F.; Li, Y.; Tseng, H. W.; Ralph, D. C.; Buhrman, R. A. *Science* **2012**, *336* (6081), 555−558.

DOI: 10.1021/acs.nanolett.5b00729
Nano Lett. XXXX, XXX, XXX−XXX

Supporting Information for

Indication of complete spin filtering in atomic-scale nickel oxide

Ran Vardimon, Marina Klionsky and Oren Tal

Department of Chemical Physics, Weizmann Institute of Science, Rehovot 76100, Israel

*Correspondence to: oren.tal@weizmann.ac.il

Contents

S1. Experimental setup

Our experiments were performed using a mechanically controllable break junction[1] setup located within a cryogenic chamber that is pumped to 10^{-5} mbar and cooled to liquid helium temperature (4.2K). The sample consists of a notched Ni wire (99.98%, 0.125mm diameter, Goodfellow) which is attached to a flexible substrate (1mm thick phosphor bronze plate covered by a 100μm thick insulating Kapton film). A three-point bending mechanism is used to bend the substrate in order to break the wire at the notch (Fig. S1). The wire is first broken under cryogenic temperatures, resulting in the exposure of two clean atomically-sharp tips. The breaking process is controlled by a piezoelectric element (PI P-882 PICMA), which is driven by a 24bit NI-PCI4461 DAQ card followed by a Piezomechanik SVR 150/1 piezo driver, allowing fast and accurate control of the relative tip displacement with sub-Angstrom resolution. An ensemble of junctions with diverse structure can be studied by repeatedly reforming the contact followed by junction breaking.

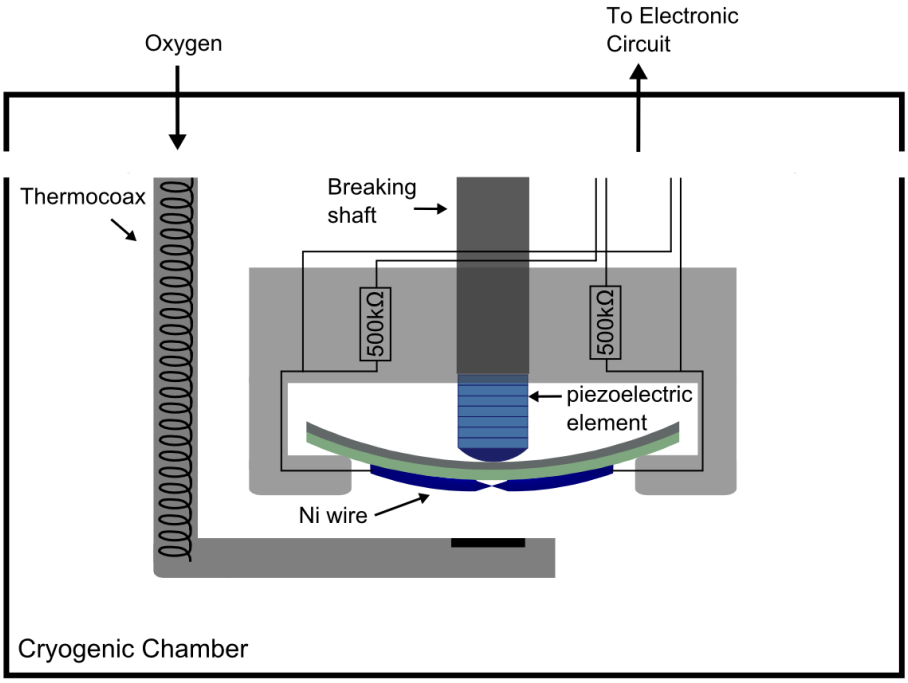

Figure S1. Schematic of the mechanically controllable break junction setup, including a heated capillary for introducing oxygen to the junction.

Measurements on bare Ni contacts lasted for a few days, in which the junction was found to exhibit the electronic characteristics of an impurity-free Ni contacts (Fig. 1c,d). Subsequently, pure oxygen gas (99.999%, Gas Technologies) was introduced to the junction via a heated capillary connecting an external molecular source with the cryogenic environment. Before measurements, the capillary was baked-out overnight at 100ºC and washed by oxygen gas several times in order to ensure that oxygen is the dominant contaminant. Once the molecule insertion procedure started, the capillary was heated in order to avoid premature condensation of the gas using a thermocoax wire running throughout its interior. The flow of oxygen was increased by slowly augmenting the pressure of oxygen (up to ~1mbar at the capillary input) and gradually heating the capillary (up to ~80K at the capillary output). The junction was monitored during the insertion process by continuously recording conductance traces. Once an indication for a change in the conductance traces was observed (i.e., Fig. 1c-f), the oxygen flow and the capillary heating were stopped.

In order to record conductance traces, the DC conductance was monitored while the contact was gradually broken by linearly increasing the voltage applied on the piezoelectric element (at a constant speed of 600nm/s and a sampling rate of 200kHz). The junction is biased with a constant voltage of 10-200mV provided by a NI-PCI4461 DAQ card. The resulting current is amplified by a current preamplifier (SR570) and recorded by the DAQ card. Following each trace the exposed atomic tips were pushed back into contact until the conductance reached a value of at least $100e^2/h$, in order to ensure that the data consists of a statistical variety of different atomic neck geometries.

Differential conductance (*dI/dV*) measurements were conducted using a standard lock-in technique. A reference sine signal of 2mVpp at ~3kHz modulating a DC bias voltage was generated by the DAQ. The AC response was recorded by the DAQ card and extracted by a LabView implemented lock-in analysis to obtain the *dI/dV* response as function of bias voltage.

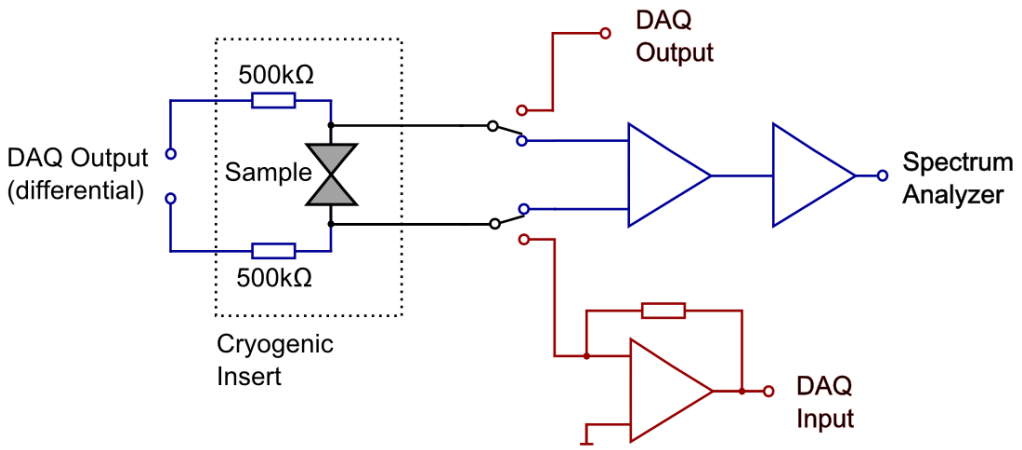

Figure S2. A scheme of the electronic circuit for conductance and shot noise measurements. The electronic circuit consists of two switchable measurement modes: Conductance Mode (red) and Noise Mode (blue).

Figure S2 shows the electronic setup connected to the sample. The circuit can be switched between a Conductance Mode, which is used to measure the DC conductance of the sample and the *dI/dV* spectra, and a Noise Mode, applied to measure the shot noise generated by the junction. In the latter mode of measurement, the relatively noisy instruments used in the Conductance Mode are disconnected to from the sample due to the high sensitivity of the shot noise measurements. The voltage noise is amplified by a differential low-noise amplifier (NF Li-75a) followed by a second voltage amplifier (Signal Recovery 5184). A power spectrum between 0-100kHz is then measured and averaged 5000 times by a fast dynamic signal analyzer (SR785). To measure shot noise, the sample is current biased by a second NI-PCI4461 DAQ card connected to the sample through two 500kΩ resistors located in proximity to the sample. The total cabling length was minimized to reduce stray capacitance to ~100pF and an additional halving of the capacitance was achieved by the differential connection.

The low level of the measured noise signal makes it sensitive to extrinsic noise. To impede noise pickup, the measurement setup was located within a Faraday cage and all instruments were connected to a specially assigned quiet ground. The amplifiers are powered by batteries to avoid noise injection from the power lines. Additionally, a RC filter was connected after the piezo driver to minimize possible excitation of mechanical noise coupled to the junction through the piezoelectric element. The RC filter was bypassed when recording conductance traces in order to avoid interference with the measurements.

Length Calibration

To determine the inter-electrode distance, the ratio k between the relative tip displacement Δx and the voltage difference applied on the piezoelectric element ΔV_p was measured. We used an established procedure based on the exponential dependence of the junction resistance on the inter-electrode displacement in the tunneling regime[2,3]. The calibration was performed for bare Ni atomic contacts, prior to the insertion of oxygen to the chamber. The calibration ratio can be determined from the relation:

$$k = \frac{\Delta x}{\Delta V_p} = \frac{\hbar}{2\sqrt{2m\phi}} \frac{\partial(lnR)}{\partial V_p}$$

where R, m, ϕ are the resistance, electron mass, and the work function of Ni, for which the bulk value of $\phi = 5.15eV$[4] was used. The value of k was calculated from fitting the resistance curves for an ensemble of 10,000 traces, recorded as the electrode apexes were brought to contact. The obtained value of k is 15±3Å/V. The variance in the calculated calibration values is attributed to the dependence of the actual work function on the different tip configurations sampled, which is a typical error for this calibration procedure[3].

S2. Characterization of nickel oxide atomic junctions

In this section, we present evidence showing that the conductance characteristics of bare Ni contacts are often observed even in the presence of oxygen, before the formation of the NiO junction, and after the broken electrodes are brought to contact. These observations indicate that both electrodes maintain their Ni character while the oxygen coverage is minor in the vicinity of the contact. Other scenarios, such as the formation of oxygen multi-layers or oxygen-induced changes of the macro-scale properties of the electrode apexes, can be ruled out. Our measurements were repeated for 3 different samples. Figure S3 presents a comparison between the statistical analyses of conductance traces performed for the three samples, after insertion of oxygen. The central features presented in the main text are reproduced for all three samples, namely: (i) the high number of counts at 2-4e^2/h for Ni and the absence of significant number of counts below (except for tunneling contributions), (ii) the appearance of frequent counts at lower conductance values after the insertion of oxygen, and (iii) the dramatic increase in junction elongation following the admittance of oxygen. This similarity indicates the reproducible formation of NiO junctions.

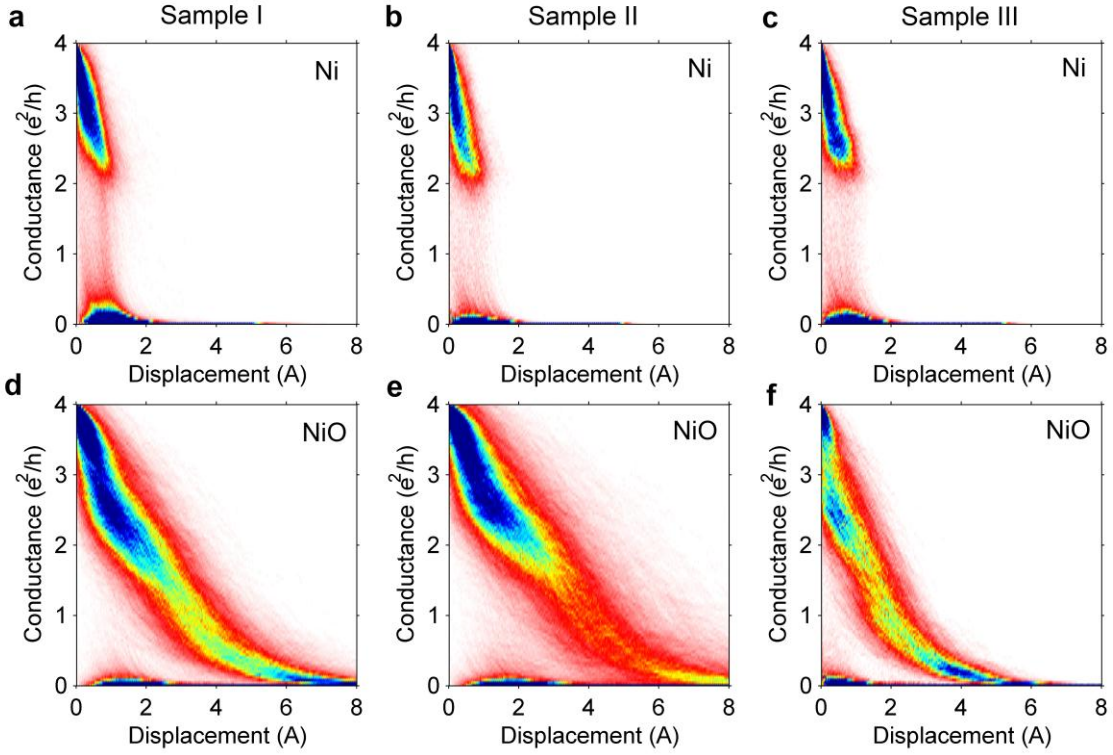

Figure S3. Conductance vs. length density plots measured for samples I (a,d), II (b,e) and III (c,e), before (a-c) and after (d-f) insertion of oxygen. The traces were aligned from the first value that drops below 4e^2/h. The density plots were constructed from 10,000 traces for the plots of sample I and from 5,000 traces for samples II and III.

The clear effect of oxygen on the conduction characteristics of the junction is well observed when the junction is pulled apart. Interestingly, when the broken tips are brought back to contact, the transport characteristics do not show a similar indication for the presence of oxygen. An example trace recorded after the insertion of oxygen is shown in Fig. S4a. The trace consists of two parts: the pull trace (blue), measured during the elongation of the junction, and the push trace (red), obtained as the tips are pushed towards each other. It can be seen that the pull trace is elongated for a larger displacement and reaches lower conductance values compared to the push trace. For the push trace, the conductance that is measured immediately after the contact is restored ($4e^2/h$) resembles that of an impurity-free single atom Ni contact[5]. This behavior is found to be robust for different traces as can be seen in Fig. S4b that presents the NiO conductance histograms constructed from the conductance values recorded for the pull (blue) and push (red) traces. The pull histogram shows frequent appearance of conductance values below $2e^2/h$, indicating the formation of NiO atomic junctions. In contrast, the histogram for push traces (red) is rather similar to the conductance histograms of bare Ni contacts (Fig. S4c), which exhibit a peak at ~$3e^2/h$ and a low number of counts below $2e^2/h$, except for the low-conductance tail, attributed to vacuum tunneling between the broken contact apexes[1]. We can therefore infer that oxygen is inserted into the junction during the pull process, but when the broken tips are brought to contact, a Ni-Ni atomic contact has a high probability to be formed. The differences between the NiO pull and push traces could be explained by surface deformation during the pulling process, promoting the mobility and eventually the insertion of oxygen in between the electrode tips, whereas the sudden contact reformation when the tips are brought together does not involve substantial surface deformation.

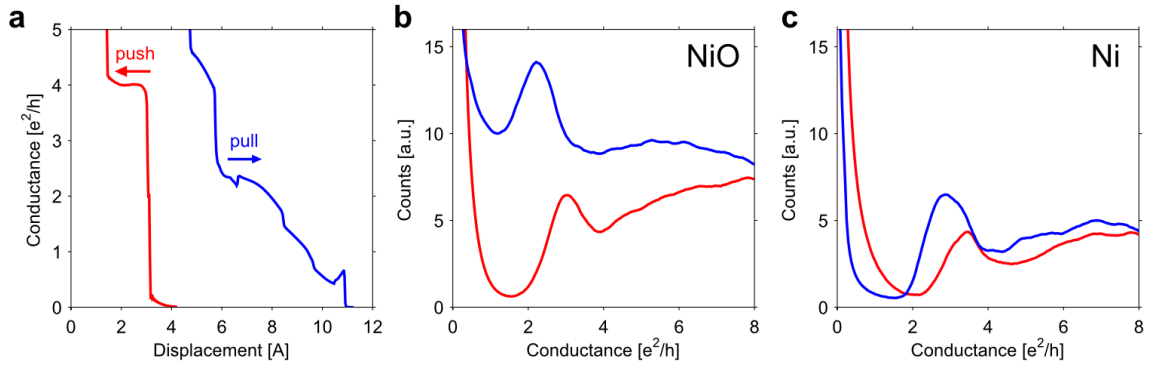

Figure S4. (a) An example trace recorded on a NiO junction, consisting of the pull trace (blue), recorded when the junction is elongated, and the push trace (red), recorded when the broken tips are brought back to contact. (b,c) Conductance histograms showing the distribution of conductance value for 10,000 pull traces (blue) and 10,000 push traces (red) for NiO (b) and bare Ni (c).

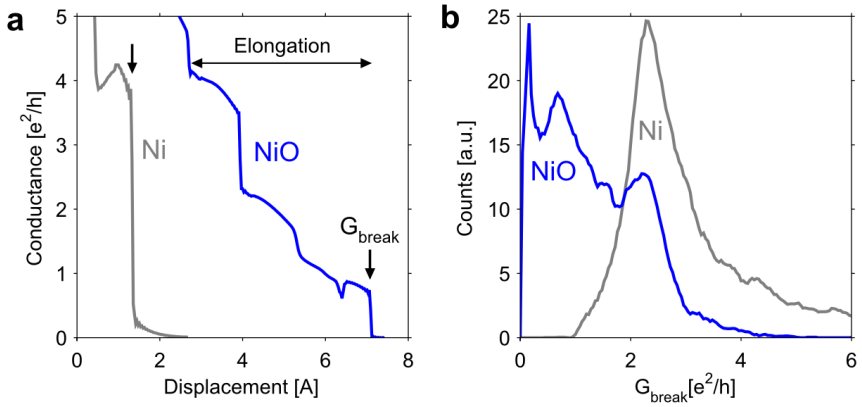

Figure S5. (a) Pull traces for Ni (grey) and NiO (blue). Arrows mark the rupture of the contact. (b) Distribution of the last conductance value measured prior to contact rupture G_{break} for bare Ni (grey) and NiO (blue) junctions. (c) Distribution of the elongations from $4e^2/h$ until rupture for bare Ni (grey) and NiO (blue) junctions.

As discussed in the main text, the final trace segments recorded for bare Ni are characterized by conductance values around 2-4e^2/h, assigned to a single-atom contact [5]. The formation of NiO junctions is indicated by the appearance of new conductance values. Yet, more information can be gained by closely inspecting the 2D conductance vs. length density plots for Ni and NiO (Fig. S3). Bare Ni contacts are found to break after an elongation of approximately 1Å, followed by low conductance reads assigned to tunneling between the broken tips (Fig. S3a-c). Tunneling contributions are also found after the insertion of oxygen (Fig. S3d-f). These contributions occur at similar displacements as the tunneling contributions observed in clean Ni contacts and are preceded by conductance values typical to a single-atom Ni contact. Therefore we infer that the junction has a certain probability to rupture from a single-atom Ni contact configuration, without the formation of a NiO junction.

To estimate the probability of forming a NiO junction, we studied the percentage of traces that show a conductance signature which is not typical for bare Ni contacts. As discussed previously, traces recorded for bare Ni do not show conductance values below ~2e^2/h, excluding vacuum tunneling contributions. Therefore, the criterion we used to identify the formation of a NiO junction was that the conductance value before rupture G_{break} is smaller than 1.8e^2/h. To obtain G_{break}, we took advantage of the appearance of a discontinuity in the conductance prior to rupture (i.e. Fig. S5a). For each trace, G_{break} was set as the conductance value appearing before the last discontinuity with a conductance difference larger than 0.1e^2/h. Using this approach, we were able to program a reliable procedure for the detection of G_{break} that is not confounded by

tunneling contributions. Figure S5b shows a comparison between the distributions of G_{break} calculated for bare Ni (grey) and NiO (blue) junctions. For the majority of traces (70%) measured after the introduction of oxygen, G_{break} is lower than 1.8e^2/h, indicating a high probability for the formation of NiO junctions.

The appearance of a peak at G_{break}=2.5e^2/h, for NiO, which corresponds to the most probable value for bare Ni, indicates that a significant percent of the contacts break from the configuration of a single-atom Ni contact. We thus conclude that the Ni character of the electrodes is maintained to a large extent after the insertion of oxygen. The modification of the transport characteristics and appearance of lower conductance values is therefore caused by the change of the atomic composition within the junction constriction.

S3. Shot noise measurements

Shot noise and differential conductance measurements were performed on different junction configurations in order to accurately obtain the Fano factor *F* and the zero-bias conductance *G*. At each junction configuration, measurements were conducted in the following order. First, the differential conductance (*dI/dV*) was measured as function of bias voltage (Fig. S6, red curve). Next, the electronic circuit was switched to Noise Mode (see section S1), and the voltage noise of the sample was measured as function of applied bias current (Fig. S7). Finally, the differential conductance spectrum (Fig. S6, blue dashed curve) was measured again by switching back to Conductance Mode to ensure that the contact configuration remained stable.

The value of *G* was set to the average differential conductance within the bias voltage window used for shot noise measurements (~4mV). The small voltage window was chosen to avoid conductance variations that could be caused by the onset of phonons. The error ΔG was determined as half the difference between the maximum and minimum differential conductance obtained within the specified bias range (illustrated in Fig. S6). Only measurements with $\Delta G < 0.04 e^2/h$ were considered for the rest of the analysis in order to ensure that the condition of unvarying transmission probabilities is met.

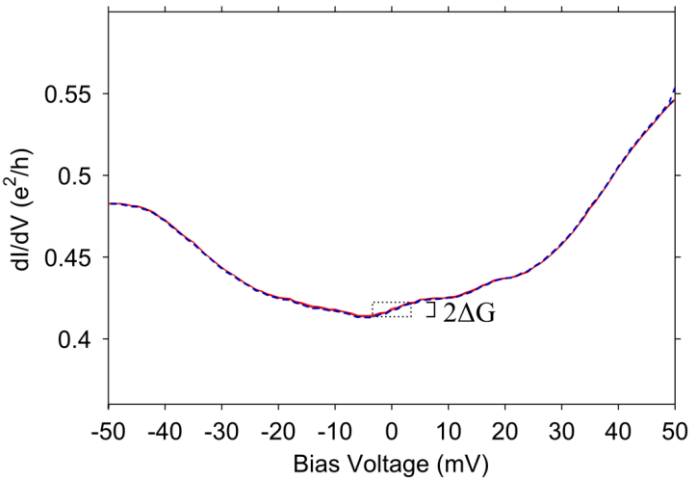

Figure S6. Differential conductance spectra measured before (red curve) and after (blue dashed curve) conducting shot noise measurements. Marked area shows the voltage window from which the zero-bias conductance (G) and error (ΔG) were calculated, corresponding to the voltage window of the shot noise measurements.

In order to obtain the Fano factor F, a series of averaged voltage noise spectra were measured as function of applied bias current (Fig. S7a). A peak-filter was applied on the data to remove spurious peaks originating from external noise sources. The voltage noise of the amplifier (1.5nV/√Hz) was measured separately as function of frequency and subtracted from the signal. In order to address the low-pass filter behavior caused by the stray capacitance, the recorded signal at zero bias is fitted to a RC transfer function and an inverse function was applied to correct the data. The corrected spectra are frequency independent within the measurement range (Fig. S7b). The current noise S_I is averaged over a selected frequency window that is free of spikes from external sources. The error ΔS_I is calculated from the standard deviation of the noise.

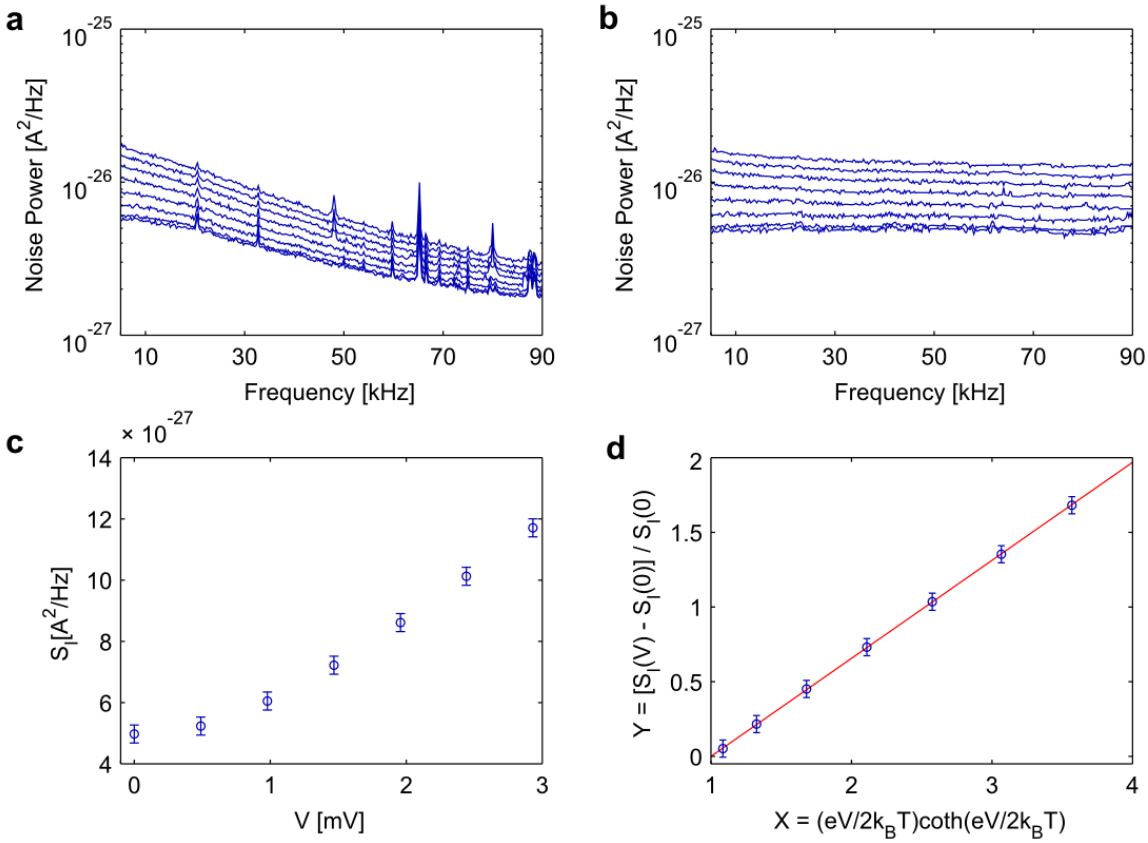

Figure S7. (a) Example noise measurements measured on a nickel-oxygen junction ($0.41e^2/h$) at different bias voltages. (b) Corrected spectra after applying a peak-filter and correcting for a fitted RC transfer function and the measured voltage noise. (c) Dependence of noise on bias voltage. The noise was averaged in a frequency window between 40-60kHz. (d) Noise dependence in reduced parameters Y(X), and a fit to eq. (2) (red line).

Figure S7c shows the dependence of the current noise S_I on the bias voltage applied across the sample. The current noise of a ballistic conductor with constant transmission probabilities vs. energy follows the expression[6]:

$$S_I(V) = 4k_BT\frac{e^2}{h}\sum_{n=1}^{N}\sum_{\sigma=\uparrow\downarrow}\tau_{n,\sigma}^2 + 2eV\coth\left(\frac{eV}{2k_BT}\right)GF \quad (1)$$

where $\tau_{n\sigma}$ are the spin-dependent transmissions probabilities of N conduction channels with $\sigma\epsilon\{\uparrow\downarrow\}$, k_B, T, e, h, V are the Boltzmann constant, temperature, electron charge, Plank constant and applied bias voltage , respectively. The above equation describes the partition noise of a quantum conductor under the assumption of constant transmission probabilities with respect to energy. For low voltages compared to the thermal energy ($eV \ll k_BT$), the formula reduces to the general Johnson-Nyquist expression for thermal noise $S_I = 4k_BTG$. At the limit of high voltage ($eV \gg k_BT$), the noise has a linear dependence on voltage $S_I(V) = 2eVGF$, reflecting the non-equilibrium noise contribution.

Following reference 7, equation (1) can be linearized by introducing the reduced parameters X and Y, such that

$$Y(V) = \frac{S_I(V) - S_I(0)}{S_I(0)}$$

$$X(V) = \frac{eV}{2k_BT}\coth\left(\frac{eV}{2k_BT}\right)$$

The resulting expression yields:

$$Y(V) = [X(V) - 1]F \quad (2)$$

Figure S7d shows the linear dependence of the data when presented in the reduced parameters. The Fano factor and its error ΔF can now be obtained from a linear fit to eq. (2). By using the reduced parameters, the fit becomes accessible in a voltage range of a few mV, where $eV \sim k_BT$ (at 4.2K, k_BT=0.36 mV). This allows reducing the voltage window used for shot noise measurements, which is useful for avoiding fluctuations of the transmission probabilities at high voltages.

S4. Shot noise measurements on Ni and NiO junctions

To test the general behavior of Ni and NiO junctions, we have measured the distribution of *F* and *G* for a large ensemble of bare Ni (Fig. S8a, squares) and NiO (circles) junctions. We start by considering the results for bare Ni contacts. The black lines divide the {*F*,*G*} space into regions for which the minimal number of spin channels is defined (see section S6). Accordingly, the distribution of data points indicates that a minimum of 3-6 channels contribute to the conductance through a single Ni atom contact, in good agreement with previous transport calculations for single-atom Ni contacts[8]. For an *sd*-metal such as Ni, up to twelve channels (six available orbitals, and a twofold factor for spin) can potentially contribute to the transport, however this number is strongly decreased as not all orbitals are in the relevant energetic window or efficiently spatially delocalized along the junction[9,10].

For NiO, the F and G distribution obtained at G=2-4e^2/h coincides with the values measured for bare Ni contacts, providing additional indication that the formation of the NiO junction begins from a single-atom Ni contact, for which the measured transport properties are not noticeably affected by the presence of oxygen absorbed on the surface.

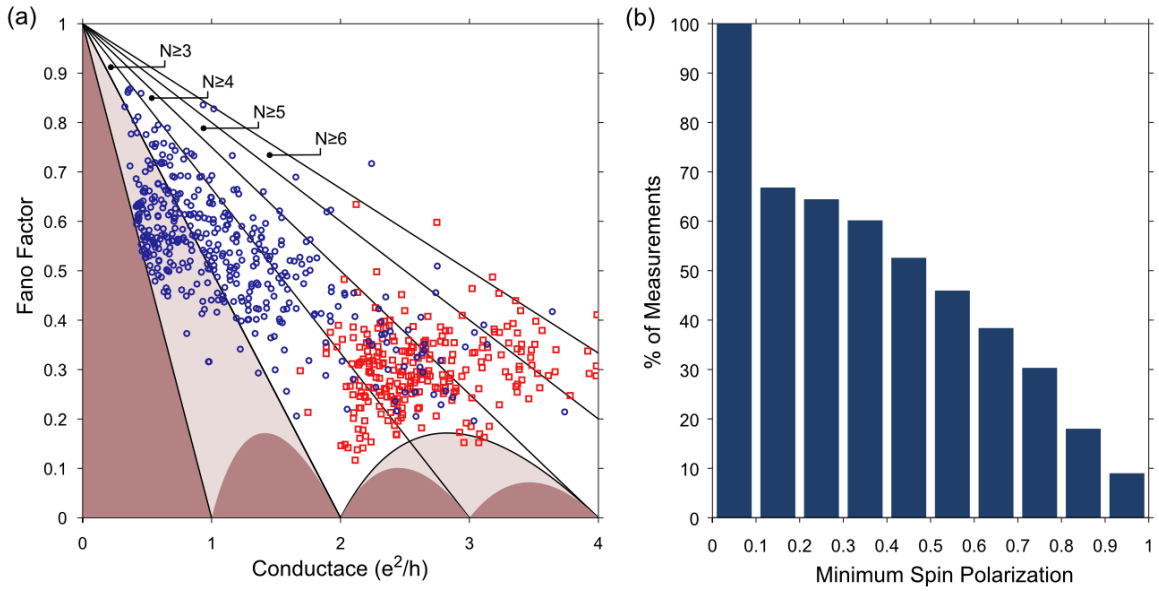

Figure S8. (a) Statistical distribution of the Fano factor (*F*) and conductance (*G*) for an ensemble of Ni (red squares) and NiO (blue circles) atomic junctions. The experimental errors for *F* and *G* do not exceed 0.04 and 0.025G_0, respectively. (b) Lower bound for spin polarization of NiO junctions, calculated from eq. (1) in main text, presented as a cumulative percentage histogram. The histogram represents 212 shot noise measurements on NiO junctions with G<1e^2/h.

At low conductance values (G<1e^2/h), associated with the formation of the NiO junction, most of the measurements are located in the restricted region, indicating a consistent tendency to feature spin-polarized transport. Figure S8b shows the cumulative distribution of the lower bound for spin polarization (P) for junctions with G<1e^2/h. A substantial degree of spin polarization is found for a significant percentage of the measurements. For example, 46% of the measurements are found to have P>50%, while 9% of the measurements show a very high spin polarization of at least 90%.

Figure 2 in the main text presents the evolution of F and G for three elongation sequences for oxygen affected nickel junctions. The detailed analysis for one of the traces is presented in Fig. 3 (main text). In figures S9 and S10 we show the channel distributions for the two other traces. The channel distribution shown in Fig. S9 shows a gradual suppression of channels along 1-2Å upon junction elongation. Figure S10 describes a sequence of measurements that starts at higher conductance. In both cases the conductance at the last stage of elongation is dominated by a single spin-channel.

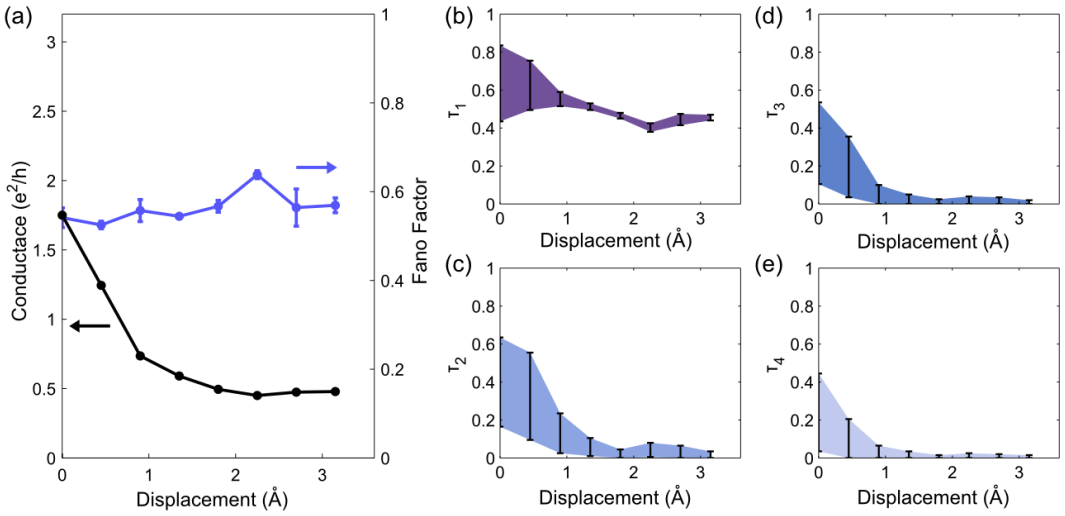

Figure S9. Channel analysis for trace 2 (pink empty circles in Figure 2 of the main text). (a) Overall conductance (black curve) and Fano factor (blue) as a function of interelectrode displacement. (b-e) The individual contributions of spin channels. The four most conducting channels are presented out of six calculated channels.

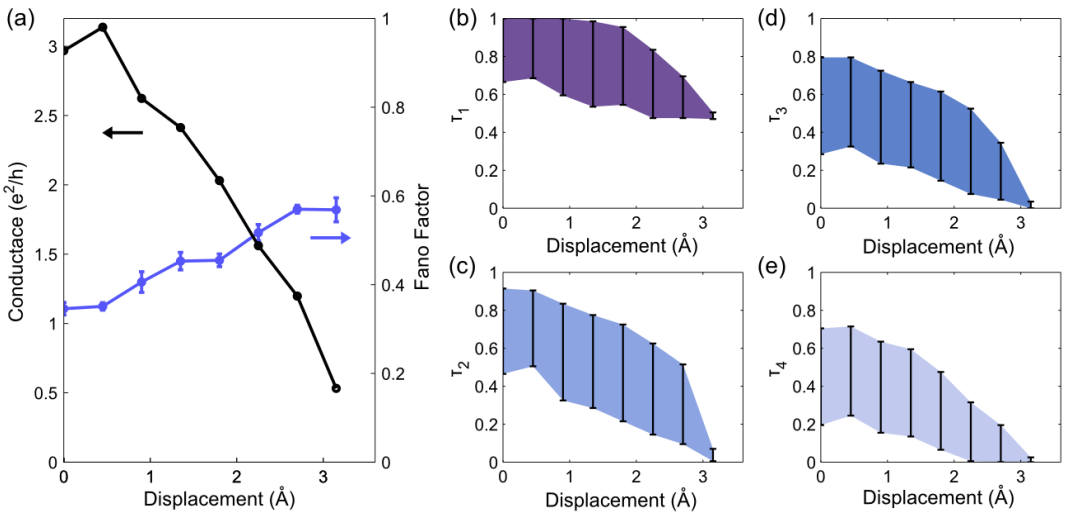

Figure S10. Channel analysis for trace 3 (purple empty triangles in Figure 2 of the main text). (a) Overall conductance (black curve) and Fano factor (blue) as a function of inter-electrode displacement. (b-e) The individual contributions of spin channels. The four most conducting channels are presented out of six calculated channels.

S5. Proof of lower bound for spin polarization

Definitions

The transmission probability for channel n ($n \in \{1 \dots N\}$) and spin type σ ($\sigma \in \{\uparrow, \downarrow\}$) is:

$$0 \leq \tau_{n\sigma} \leq 1$$

The conductance (in units of e^2/h) and the Fano factor are:

$$G = \sum_{n\sigma} \tau_{n\sigma}$$

$$F = \frac{\sum_{n\sigma} \tau_{n\sigma}(1 - \tau_{n\sigma})}{\sum_{n\sigma} \tau_{n\sigma}} = 1 - \frac{\sum_{n\sigma} \tau_{n\sigma}^2}{G}$$

The absolute spin polarization is defined as:

$$P = \frac{|\sum_n \tau_{n\uparrow} - \sum_n \tau_{n\downarrow}|}{G}$$

For the case of two channels of opposite spin, $T_\uparrow, T_\downarrow$, there is a unique solution that yields a given combination of F and G, which can be obtained by solving:

$$T_\uparrow + T_\downarrow = G$$

$$T_\uparrow^2 + T_\downarrow^2 = G(1 - F)$$

we assume without loss of generality that:

$$T_\uparrow \geq T_\downarrow$$

The absolute spin polarization therefore equals:

$$P^{2ch} = \frac{T_\uparrow - T_\downarrow}{G} = \frac{2T_\uparrow - G}{G}$$

Theorem

For any possible set of transmission probabilities $\{\tau_{n\sigma}\}$ that satisfies F and G, the resulting absolute spin polarization P obeys:

$$P \geq P^{2ch}$$

Proof

We assume by contradiction that there exists a set $\{\tau_{n\sigma}\}$ that satisfies F and G and that its absolute spin polarization is such that:

$$P < P^{2ch}$$

We assume without loss of generality that:

$$\textbf{(i)} \qquad \sum_n \tau_{n\uparrow} \geq \sum_n \tau_{n\downarrow}$$

The absolute spin polarization can therefore be written as:

$$P = \frac{\sum_n \tau_{n\uparrow} - \sum_n \tau_{n\downarrow}}{G} = \frac{2\sum_n \tau_{n\uparrow} - G}{G}$$

Since $P < P^{2ch}$ then:

$$\frac{2\sum_n \tau_{n\uparrow} - G}{G} < \frac{2T_\uparrow - G}{G}$$

And therefore:

$$\textbf{(ii)} \qquad T_\uparrow > \sum_n \tau_{n\uparrow}$$

For the case of two spin-channels we have the equality:

$$G(1-F) = T_\uparrow^2 + T_\downarrow^2 = T_\uparrow^2 + (G - T_\uparrow)^2 = 2T_\uparrow^2 - 2GT_\uparrow + G^2$$

On the other hand:

$$G(1-F) = \sum_n \tau_{n\uparrow}^2 + \sum_n \tau_{n\downarrow}^2 \leq (\sum_n \tau_{n\uparrow})^2 + (\sum_n \tau_{n\downarrow})^2$$

$$= (\sum_n \tau_{n\uparrow})^2 + (G - \sum_n \tau_{n\uparrow})^2 = 2(\sum_n \tau_{n\uparrow})^2 - 2G(\sum_n \tau_{n\uparrow}) + G^2$$

Comparing both expressions for $G(1-F)$ yields the following inequality:

$$2T_\uparrow^2 - 2GT_\uparrow + G^2 \leq 2(\sum_n \tau_{n\uparrow})^2 - 2G(\sum_n \tau_{n\uparrow}) + G^2$$

$$T_\uparrow^2 - GT_\uparrow \leq (\sum_n \tau_{n\uparrow})^2 - G(\sum_n \tau_{n\uparrow})$$

$$0 \leq (\sum_n \tau_{n\uparrow})^2 - T_\uparrow^2 + GT_\uparrow - G(\sum_n \tau_{n\uparrow})$$

$$0 \leq (\sum_n \tau_{n\uparrow} - T_\uparrow)(\sum_n \tau_{n\uparrow} + T_\uparrow) + G(T_\uparrow - \sum_n \tau_{n\uparrow})$$

$$\textbf{(iii)} \qquad 0 \leq (T_\uparrow - \sum_n \tau_{n\uparrow})(G - \sum_n \tau_{n\uparrow} - T_\uparrow)$$

However, from **(ii)** we know that:

$$(T_{\uparrow} - \sum_n \tau_{n\uparrow}) > 0$$

And from **(i)** and **(ii)**:

$$(G - \sum_n \tau_{n\uparrow} - T_{\uparrow}) \ < (G - \sum_n \tau_{n\uparrow} - \sum_n \tau_{n\downarrow}) = 0$$

Implying that:

$$(T_{\uparrow} - \sum_n \tau_{n\uparrow})(G - \sum_n \tau_{n\uparrow} - T_{\uparrow}) < 0$$

Therefore we have a contradiction with **(iii)**.

End of Proof.

S6. Proof of maximum Fano factor for a fixed number of channels

Definitions

The transmission probability for channel n ($n \in \{1 \dots N\}$) is:

$$0 \leq \tau_n \leq 1$$

For a simple and general notation, we do not specify the spin type of each channel.

The conductance (in units of e^2/h) and the Fano factor are:

$$G = \sum_n \tau_n$$

$$F = \frac{\sum_n \tau_n(1-\tau_n)}{\sum_n \tau_n} = 1 - \frac{\sum_n \tau_n^2}{G}$$

Theorem

The maximum value of F for a given number of channels N and a given conductance G is

$$F_{max} = 1 - \frac{G}{N}$$

Proof

If all channels have equal transmission, then:

$$\tau_n = \frac{G}{N}$$

And the Fano factor is:

$$F = 1 - \frac{1}{G}\sum_{n=1}^{N}\left(\frac{G}{N}\right)^2 = 1 - \frac{G}{N} = F_{max}$$

We can express any distribution of transmission probabilities as:

$$\tau_n = \frac{G}{N} + x_n$$

Such that $-\frac{G}{N} \leq x_n \leq 1 - \frac{G}{N}$. To satisfy the given conductance G, we demand:

$$(\boldsymbol{i}) \qquad \sum_{n=1}^{N} x_n = 0$$

The Fano Factor will be:

$$F = 1 - \frac{1}{G}\sum_{n=1}^{N}\left(\frac{G}{N} + x_n\right)^2$$

$$= 1 - \frac{1}{G}\left[\sum_{n=1}^{N}\left(\frac{G}{N}\right)^2 + \sum_{n=1}^{N} x_n^2 + 2\frac{G}{N}\sum_{n=1}^{N} x_n\right]$$

using **(i)**:

$$F = 1 - \frac{G}{N} - \frac{1}{G}\sum_{n=1}^{N} x_n^2$$

Since $x_n^2 \geq 0$ we obtain:

$$F \leq 1 - \frac{G}{N} = F_{max}$$

End of Proof.

References

(1) Muller, C. J.; van Ruitenbeek, J. M.; de Jongh, L. J. *Phys. C Supercond.* **1992**, *191*, 485–504.
(2) Kolesnychenko, O. Y.; Shklyarevskii, O. I.; van Kempen, H. *Rev. Sci. Instrum.* **1999**, *70*, 1442–1446.
(3) Untiedt, C.; Yanson, A. I.; Grande, R.; Rubio-Bollinger, G.; Agraït, N.; Vieira, S.; van Ruitenbeek, J. M. *Phys. Rev. B* **2002**, *66*, 085418.
(4) Michaelson, H. B. *J. Appl. Phys.* **1977**, *48*, 4729–4733.
(5) Untiedt, C.; Dekker, D. M. T.; Djukic, D.; van Ruitenbeek, J. M. *Phys. Rev. B* **2004**, *69*, 081401.
(6) Blanter, Y. M.; Büttiker, M. *Phys. Rep.* **2000**, *336*, 1–166.
(7) Kumar, M.; Avriller, R.; Yeyati, A. L.; van Ruitenbeek, J. M. *Phys. Rev. Lett.* **2012**, *108*, 146602.
(8) Pauly, F.; Dreher, M.; Viljas, J. K.; Häfner, M.; Cuevas, J. C.; Nielaba, P. *Phys. Rev. B* **2006**, *74*, 235106.
(9) Cuevas, J. C.; Yeyati, A. L.; Martin-Rodero, A. *Phys. Rev. Lett.* **1998**, *80*, 1066–1069.
(10) Jacob, D.; Fernández-Rossier, J.; Palacios, J. J. *Phys. Rev. B* **2005**, *71*, 220403.